PCCP

PAPER

View Article Online
View Journal | View Issue

Cite this: *Phys. Chem. Chem. Phys.*, 2023, **25**, 10749

The contribution of phonons to the thermal expansion of some simple cubic hexaboride structures: SmB_6, CaB_6, SrB_6 and BaB_6†

Li Li, [a] Keith Refson [b] and Martin T Dove *[cde]

Received 30th January 2023,
Accepted 24th March 2023

DOI: 10.1039/d3cp01306e

rsc.li/pccp

We have performed first-principles calculations of the structure and lattice dynamics in the metal hexaborides SmB_6, CaB_6, SrB_6 and BaB_6 using Density Functional Theory in an attempt to understand the negative thermal expansion in the first of these materials. The focus is on the role of Rigid Unit Modes involving rotations of the B_6 octahedra similar to the rotations of structural polyhedra connected by bonds in $Zn(CN)_2$, Prussian Blue and $Si(NCN)_2$. However, it was found that there is very low flexibility of the network of connected B_6 octahedra, and the lattice dynamics do not support negative thermal expansion except possibly at very low temperature. Thus the negative thermal expansion observed in SmB_6 probably has an electronic origin.

1 Introduction

The simple cubic hexaborides XB_6, which are formed from some transition metals (X = Sm, Y, La for example) and some alkali earth elements (X = Ca, Sr, Ba) are shown in Fig. 1.[1,2] The crystal structure consists of B_6 octahedra, linked together by B–B bonds. This is similar to the cubic perovskite structure, but without the octahedral cation, and more importantly with the shared oxygen atom replaced by a B–B bond. In this sense it is like $Zn(CN)_2$,[3] which has Zn-centred tetrahedra connected by shared CN bonds, and even more similar to analogues of Prussian Blue in which metal-centred octahedra are connected by shared CN bonds in exactly the same topological layout.[4,5] The main difference is that the essential network in SmB_6 is entirely made from boron atoms, rather than metal-centred oxide or halide polyhedra, and thus cubic metal hexaboride materials potentially represent a new type of network material.

Over the past two decades we have seen a rapid increase in the number of conventional network materials that show negative thermal expansion (NTE), that is, over a range of temperatures the material will shrink rather than expand on heating.[6–9] Many of these materials are oxides or analogues based on replacing the oxygen anion by a halogen anion or even a molecular anion.[10] In these cases there are structural polyhedra that are connected at corners to form infinite networks. Examples are ReO_3,[11,12] and its analogue ScF_3,[13,14] $Zn(CN)_2$[3] as

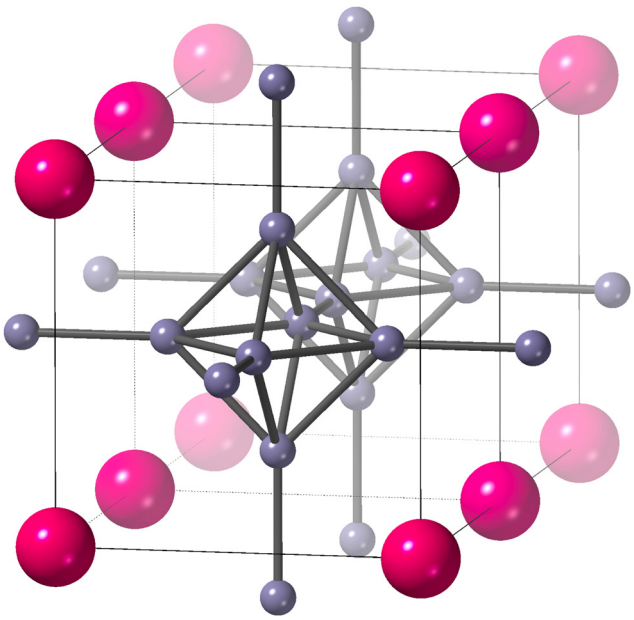

Fig. 1 The crystal structure of SmB_6 (space group $Pm\bar{3}m$, lattice parameter 4.134 Å at temperature of 20 K).[1] B atoms are the small grey bonded spheres, and Sm atoms are the larger pink atoms at the corners of the unit cell.

[a] College of Science, Civil Aviation Flight University of China, 46 Nanchang Road, Guanghan, Sichuan, 618307, China
[b] ISIS Facility, Harwell Campus, Chilton, Didcot, OX11 0QX, UK
[c] College of Computer Science, Sichuan University, Chengdu, Sichuan, 610065, China. E-mail: martin.dove@icloud.com
[d] School of Mechanical Engineering, Dongguan University of Technology, 1st Daxue Road, Songshan Lake, Dongguan, Guangdong, 523000, China
[e] School of Physical and Chemical Sciences, Queen Mary University of London, Mile End Road, London, E1 4NS, UK

† Electronic supplementary information (ESI) available. See DOI: https://doi.org/10.1039/d3cp01306e

an analogue of the cubic cristobalite phase of SiO_2, and the most famous NTE material ZrW_2O_8[15] with corner linked WO_4 tetrahedra and ZrO_6 octahedra.

NTE in network materials is commonly associated with a mechanism known as the 'tension effect'.[8] One simple example is cubic ScF_3.[16] The crystal structure has cubic symmetry, and consists of corner-sharing ScF_6 octahedra with linear Sc–F–Sc bonds – essentially it has the cubic perovskite structure without the 12-coordinated cation. The Sc–F bonds are relatively rigid (and have positive thermal expansion), and so rotations of the Sc–F bonds will necessarily reduce the corresponding Sc–Sc distances and hence will lead to overall reduction in the crystal size. Such rotations occur as thermally-excited vibrational motions, and their effect in reducing the Sc–Sc distance exceeds that from the thermal expansion of the Sc–F bonds.[14,16] Thus the effect becomes larger with higher temperature, leading directly to NTE. Because atomic motions are correlated, the important question is the extent to which the structure allows for low-frequency rotational vibrations. In structures consisting of connected polyhedra, the question becomes focussed on the balance between the phonons in which the polyhedra rotate as nearly-rigid objects – the Rigid Unit Modes (RUMs)[17,18] – and the phonons that lead to bending of the bonds of polyhedra. This point has been discussed in detail elsewhere.[19]

Of the metal hexaborides, as far as we can tell low-temperature lattice parameters have only been measured for SmB_6, which itself is now best known as a topological insulator.[20–28] Experimental data show the existence of NTE in SmB_6 at low temperatures,[1] and we have recently confirmed this with our own diffraction data shown in Fig. 2. On the other hand, there are higher-temperature data for other metal hexaborides, which all show positive thermal expansion above room temperature.[2]

In this paper we investigate the role of phonons and the standard Grüneisen and tension effect mechanisms[8] using density functional theory simulations of SmB_6 and analogue materials with alkaline earth cations, CaB_6, SrB_6 and BaB_6. In fact it will be shown here that although there is a phonon mechanism to generate NTE, it is not sufficient in these materials to give NTE over a wide range of temperatures. In the case of SmB_6 it is impossible to reproduce the observed NTE from a phonon mechanism, and thus we will conclude that the mechanism for NTE in SmB_6 may more likely have an electronic origin.

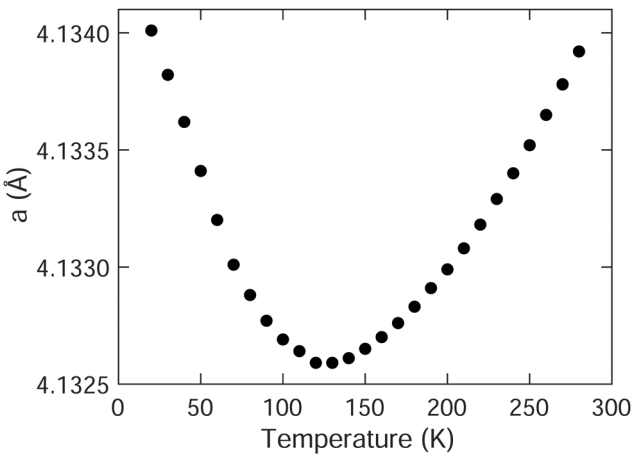

Fig. 2 Unpublished experimental data for the temperature-dependence of the lattice parameter of SmB_6, obtained by the corresponding author with Zhongsheng Wei and Dean Keeble at the XPDF beam line at the Diamond synchrotron facility in the UK.

2 Methods

2.1 DFT methods

Simulations were performed using the CASTEP program,[29] version 19. This uses a density-functional-theory method based on periodic structures that make use of plane-wave basis sets. The effects of core electrons were handled using norm-conserving pseudopotentials supplied as part of the CASTEP package (NCP19).

The calculations were performed using the standard PBE generalised-gradient approximation[30,31] for CaB_6, SrB_6 and BaB_6, assuming the electronic states are those of an insulator. The integration of the electronic states was performed using a Monkhorst–Pack grid[32] of $7 \times 7 \times 7$ wave vectors. A cut-off energy of 800 eV was chosen for the plane wave electronic basis set based on convergence tests for energy differences. For structure optimisation, calculations were performed to a convergence of energies to 10^{-8} eV per atom, convergence of force to 10^{-4} eV Å^{-1}, and convergence of stress to 10^{-4} GPa. All limits were chosen on the basis of tests on convergence of energy differences for two similar volumes.

For the calculations on SmB_6, on the other hand, the system was treated as a metal. A cut-off energy of 900 eV was used for the electronic basis set. Other details were the same as for the other materials.

We did not consider contributions from magnetic spin moments because it has been shown that SmB_6 remains non-magnetic down to very low temperatures.[21]

2.2 Structure optimisation

The optimised values of the lattice parameters and interatomic distances for all systems are compared with experimental data,[1,33] in Table 1. In each case agreement on lattice parameters is good, to within 1%.

The bond distances are shown in Fig. 3, where we are able to make one important point. Increasing the size of the metal atom clearly, from Table 1, creates some strain in the crystal structure. This strain is accommodated mostly by expansion of the length of the B–B bond connecting two octahedra, and to a much lesser extent by increasing the size of the octahedra.

2.3 Phonon methods

Phonon frequencies for the alkali earth hexaborides were calculated using the density functional perturbation theory (DFPT) method.[34,35] An interpolation method was used to compute frequencies for any wave vector based on calculations of the

Table 1 Calculated and experimental crystal structure data for the four hexaborites examined in this study. *a* is the cubic lattice parameter, and *x* is the fractional coordinate of the boron atom. Bond length values are in Å. B–B (1) is the bondlength within the B_6 octahedra, and B–B (2) is the bondlength between octahedra. M–B is the bond length between the metal cation and the nearest boron atom. Experimental data from SmB_6 are from the neutron diffraction measurements of Trounov *et al.*[1] measured at a temperature of 23 K, and for the other phase data are taken from a compilation of Schmitt *et al.*[33] for measurements performed at room temperature

	a (Å)	B *x*	B–B (1)	B–B (2)	M–B
SmB_6 exp	4.133	0.200	1.755	1.652	3.037
SmB_6 calc	4.129	0.200	1.752	1.652	3.034
CaB_6 exp	4.152	0.202	1.750	1.677	3.053
CaB_6 calc	4.122	0.203	1.732	1.673	3.032
SrB_6 exp	4.198	0.203	1.764	1.704	3.088
SrB_6 calc	4.194	0.203	1.762	1.702	3.085
BaB_6 exp	4.276	0.205	1.784	1.753	3.148
BaB_6 calc	4.262	0.206	1.775	1.752	3.138

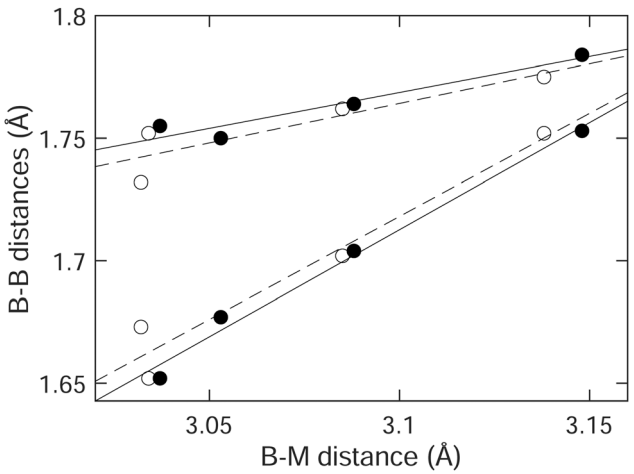

Fig. 3 Comparison of the two experimental[1,33] (filled circles) and calculated (open circles) B–B distances in the four hexaborides, plotted as a function of the metal (M) to boron distance. From left to right the metal atoms are Sm, Ca, Sr and Ba. Note that there is a close overlap of the experimental and calculated distances in the case of the SrB_6. The upper data are for the B–B distances within the octahedra and the lower data are for B–B distances connecting two octahedra. The lines are fits to the data, and highlight the fact that most of the strain imposed by increasing the size of the metal atom is accommodated though expansion of the B–B bond connecting two octahedra.

dynamical matrices performed for a Monkhorst–Pack grid of wave vectors of size $7 \times 7 \times 7$ in reciprocal space. A convergence tolerance for force constants during the DFPT calculations of 10^{-5} eV Å^{-2} was used. The phonon acoustic sum rule was enforced. For SmB_6 the dynamical matrix was calculated using a supercell method. We have checked in the case of CaB_6 that the two methods give substantially the same results.

Volumetric thermal expansion[8] is given by the formula $\alpha_V = C_V\bar{\gamma}/BV$, where C_V is the heat capacity at constant volume, and $B = V\partial P/\partial V$ is the bulk modulus. The key quantity is the overall Grüneisen parameter $\bar{\gamma}$, which can be constructed from the individual mode Grüneisen parameters defined as $\gamma_i = (\partial\omega_i/\partial V) \times (V/\omega_i)$, where ω_i is the angular frequency of the phonon labelled i and V is the crystal volume. The overall Grüneisen parameter is formed as

$$\bar{\gamma} = \frac{1}{C_V}\sum_i \hbar\omega_i \frac{\partial n(\omega_i, T)}{\partial T}\gamma_i \quad (1)$$

where $n(\omega_i, T)$ is the normal Bose–Einstein distribution.

For each system a set of calculations was performed with the crystal structure in its lowest-energy configuration, then a second set of calculations was performed using a lattice parameter expanded by about 1%. Mode Grüneisen parameters were obtained as $\gamma_i = (\Delta\omega_i/\omega_i)/(\Delta V/V)$ from lattice dynamics calculations using a set of random wave vectors. An eigenvector-matching algorithm[36] was used to ensure that the correct pairs of modes were compared in the calculation of $\Delta\omega_i$. C_V was calculated from the phonon frequencies using the standard formula based on differentiation of the Bose–Einstein distribution function.

3 Phonon dispersion curves of CaB_6 and SmB_6

Here we consider the main details of the phonon dispersion curves. These are shown for SmB_6 and CaB_6 along the main symmetry directions in reciprocal space in Fig. 4. Corresponding data for SrB_6 and BaB_6 are given in the ESI.†

At zero wave vector, the mode decomposition gives acoustic modes with irreducible representation T_{1u}, and $A_{1g} + E_g + T_{1g} + T_{2g} + 2T_{1u} + T_{2u}$ for the optic modes. In CaB_6 the two optic T_{1u} modes show splitting of the frequencies of the longitudinal and transverse modes, which is not present in SmB_6 because in this case it is a metal. The values of frequencies at zero wave vector are given in Table 2.

Images of the mode eigenvectors are shown in the ESI.† The lowest frequency T_{1u} mode involves simple opposite displacements of the metal cation and B_6 octahedron, creating a local electrical dipole moment. The T_{2u} mode consists of sideways displacements of the B–B bond connecting two octahedra in the perpendicular direction. This necessarily causes deformation of the B_6 octahedra. The T_{1g} mode involves the rotation of the B_6 octahedra without distortion (see the discussion in Section 4), together with a counter rotation of the linking B–B bonds. The higher-frequency T_{1u} mode involves displacements of the linking B–B bond along the direction of the bond, causing bond-bending distortions of the B_6 octahedra. The E_g mode involves asymmetric stretching of the B–B bonds within the B_6 octahedra. Finally, the A_{1g} mode is the totally-symmetric stretch of all bonds within the B_6 octahedra accompanied by an opposite contraction of the linkage B–B bonds.

The low-frequency part of the dispersion curves of SmB_6 have been measured by inelastic neutron scattering along the three symmetry directions from zero wave vector at room temperature.[37] The measurements included the acoustic modes in each direction, and the lowest set of optic modes that come together as the T_{1u} triplet at just below 5 THz at zero wave vector. Agreement between calculation and experiment is

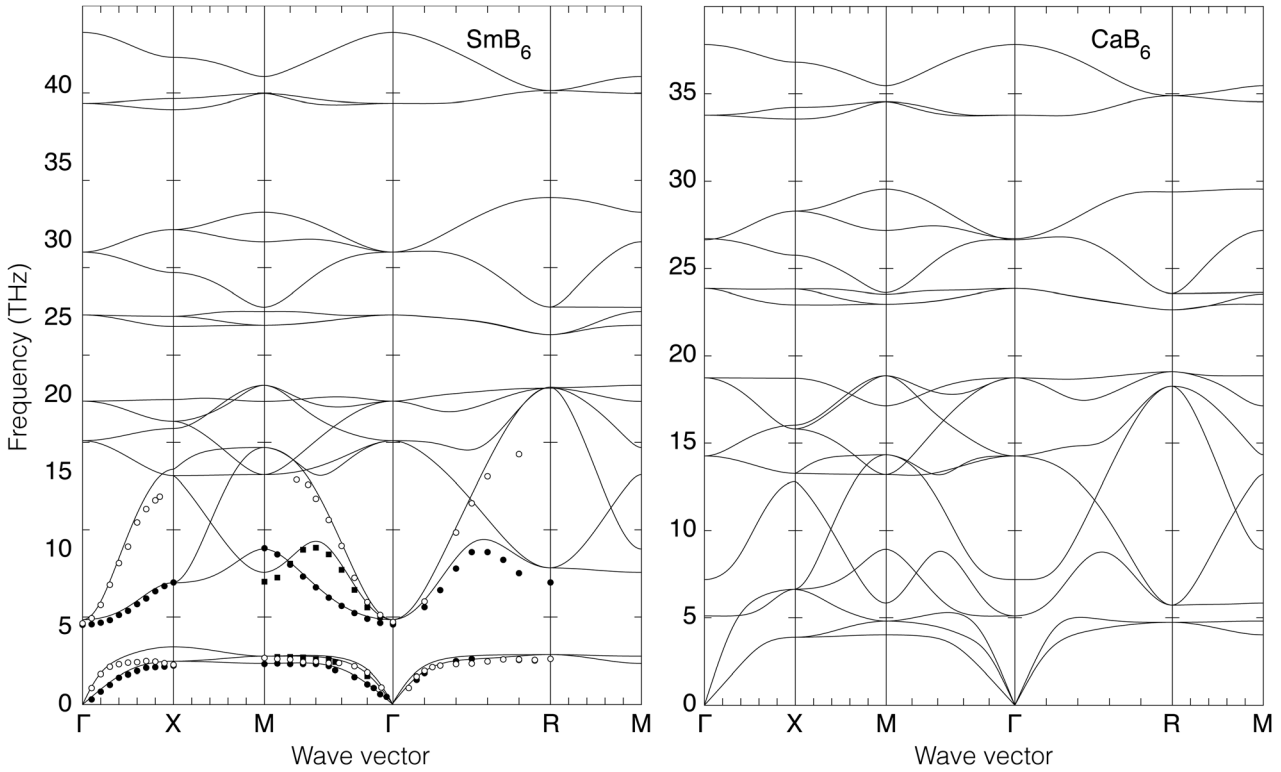

Fig. 4 Calculated phonon dispersion curves of SmB_6 (left) and CaB_6 (right). The wave vector labels have conventional meaning: Γ represents the wave vector (0, 0, 0), X represents $(\frac{1}{2}, 0, 0)$, M represents $(\frac{1}{2}, \frac{1}{2}, 0)$ and R represents $(\frac{1}{2}, \frac{1}{2}, \frac{1}{2})$. Results from a single-crystal neutron inelastic scattering experiment[37] are represented as points, using different symbols to aid clarity.

Table 2 Calculated phonon frequencies for the four metal hexaborides of this study, SmB_6, CaB_6, SrB_6 and BaB_6 at zero wave vector, in units of THz. In each case other than SmB_6, which are ionic insulators, the T_{1u} modes show longitudinal/transverse splitting, and we give the frequencies of both components together. As a metal, SmB_6 does not show this splitting

Mode	SmB_6	CaB_6	SrB_6	BaB_6
T_{1u}	4.86	5.15, 7.22	4.68, 6.27	5.63, 6.79
T_{2u}	15.11	14.32	14.10	13.80
T_{1g}	17.37	18.76	18.41	18.52
T_{2g}	22.32	23.93	23.31	22.50
T_{1u}	25.94	26.73, 26.80	25.84, 25.90	24.86, 24.93
E_g	34.44	33.94	32.33	29.72
A_{1g}	38.50	37.99	36.33	33.54

excellent, including the lack of LO/TO splitting of the T_{1u} modes at zero wave vector, the significant flattening of acoustic mode dispersion curves, the subtle cross-over of the transverse and longitudinal acoustic modes for wave vectors around $(\frac{1}{4}, \frac{1}{4}, 0)$ (half way between the points labelled Γ and M in Fig. 4), the rapid rise of the acoustic modes in increasing wave vector from zero wave vector (Γ), and the maxima in the frequencies of the low-frequency optic modes at the points $(\frac{1}{4}, \frac{1}{4}, 0)$ (half way between Γ and M) and $(\frac{1}{4}, \frac{1}{4}, \frac{1}{4})$ (half way between Γ and R). The calculated frequencies of the acoustic modes are in excellent agreement with experiment across the whole Brillouin zone for all three directions. The lowest frequency TO modes agree very well with experiment, including the values of the maximum frequencies. The maximum frequencies of the low-frequency LO modes are calculated to have slightly higher frequencies than experiment at the zone boundaries, but the fact that the frequency of the LO mode at wave vector X is lower than that at wave vector M, which in turn is lower than that at wave vector R, is reproduced in the calculation. On the basis of this level of agreement between calculation and experiment we conclude that our DFT approach is reproducing most of the relevant behaviour of the phonon dispersion curves.

For SmB_6 and CaB_6 we can compare the calculated frequencies for zero wave vector with the results from Raman spectroscopy,[25,38] as summarised in Table 3. We consider the agreement to be good.

It is interesting to draw attention to the phonon anti-crossing at low frequencies, involving the acoustic and low-lying optic modes.

Table 3 Experimental and calculated Raman frequencies, given in the units of measurement, cm^{-1}. Experimental data for SmB_6 are from Nyhus *et al.*[25] (older data are given by Mörke *et al.*[39]), and were measured at a temperature of 300 K. Experimental data for CaB_6 are from Ogita *et al.*,[38] and were measured at a temperature of 13 K. The exact agreements of pairs of values are coincidental

Mode	SmB_6 Expt	SmB_6 Calc	CaB_6 Expt	CaB_6 Calc
A_{1g}	1280	1284	1291	1264
E_g	1148	1148	1149	1129
T_{2g}	730	743	780	780

Table 4 Values of elastic constants C_{11}, C_{44} and C_{12}, and bulk modulus B, deduced from the slopes of the acoustic modes in the limit of small wave vector as described in the ESI

	C_{11} (GPa)	C_{44} (GPa)	C_{12} (GPa)	B (GPa)
SmB_6	440	71	22	161
CaB_6	433	54	14	153
SrB_6	394	66	52	166
BaB_6	418	98	34	162

This is particularly evident in the directions Γ–X, where as a result both the transverse and longitudinal acoustic modes are seen to flatten quickly on increasing wave vector, and the optic modes rise sharply. The effect is much larger in SmB_6 than in CaB_6, leading to lower frequencies at the X point in SmB_6. The same effect is seen in other directions Γ–M and Γ–R. It is noticeable that in each case the extrapolation to the zone boundary of the un-crossed acoustic modes gives similar frequencies.

It is also noticeable from Table 2 that there is a significant and consistent decrease in the calculated value of the A_{1g} symmetric stretch mode from SmB_6 to BaB_6. This is commensurate with a change in B–B bond lengths (Table 1), that is the longer bond has a weaker force constant. However, this trend is not seen in the independent data for SmB_6 and CaB_6 shown in Table 3, for reasons that are not clear.

The slopes of the acoustic modes were used to calculate the elastic constants and bulk modulus. The method is described in the ESI,† and key data are provided there. The results are shown in Table 4. The results for SmB_6, CaB_6 and SrB_6 are consistent with results given by the Materials Project as computed from analysis using finite strains, although data for BaB_6 are not available there.

4 Flexibility analysis

The Rigid Unit Modes (RUMs)[17,18] discussed previously in regard to framework structures composed of corner-linked structural polyhedra, such as silicate and perovskite structures, are the phonons that can propagate without any distortion of the polyhedra. In the case of oxides with corner-sharing polyhedra, the RUMs typically propagate with low frequency. The concept of RUMs can be extended to systems composed of structural polyhedra connected *via* a shared molecular ligand, as in the related materials $Zn(CN)_2$[3,40] and $Si(NCN)_2$,[41] or analogues of Prussian Blue, $Fe_4^{III}[Fe^{II}(CN)_6]_3$.[40] However, as was found in the case of $Zn(CN)_2$, the RUMs that involve bending of the linear Zn–CN–Zn linkage have relatively high frequency, so one should not assume that in these extended network systems the RUMs will have low frequencies,[3] which is the pertinent issue for the cubic metal hexaborides.

We have evaluated all possible RUMs for the cubic metal hexaboride structure, based on rigid-body motions of the B_6 octahedra and with a rigid connecting B–B bond, and disregarding any role of the metal atoms. We begin with a simple count of degrees of freedom and constraints. Each octahedron has 6 degrees of freedom. Each connecting B–B provides one constraint, which is shared between the two connected octahedra. Thus we have 3 constraints for each octahedron. The difference between the numbers of degrees of freedom and constraints implies there are three RUMs for each wave vector, a result confirmed by calculation using a dynamical matrix. It is often found that symmetry leads to the presence of additional RUMs at special wave vectors, and this was found to be the case here using a simple flexibility mode (discussed below). The key results are given in Table 5, and are consistent with those obtained by Goodwin[40] for the analogous Prussian Blue crystal.

Table 5 Number of RUMs for special wave vectors. For all other wave vectors, including the general wave vector without symmetry, the number of RUMs is equal to 3

Wave vector	Number of RUMs
(0, 0, 0)	6
(ξ, 0, 0)	5
(1/2, 0, 0)	5
(1/2, ξ, 0)	4
(ξ, ξ, 0)	4
(1/2, 1/2, 0)	4
(ξ, ζ, 0)	4

The additional three RUMs at wave vector $\mathbf{k} = (0, 0, 0)$ are the trivial acoustic modes. The rest of the results given in Table 5 can be accounted for simply by noticing that there are planes of wave vectors of the form (ξ, ζ, 0) containing one additional RUM each. Thus, for example, the wave vector (ξ, 0, 0) lies on the intersection of two such planes and thus has an additional two RUMs, as seen in Table 5. This mode is a shear acoustic mode.

To map the RUMs onto the phonon dispersion curves, we use the rigidity analysis described previously by Rimmer and Dove.[36] The eigenvectors from a full lattice dynamics calculation are compared with those from a calculation with a model designed to reproduce the spectrum of RUMs. The calculations were performed using the GULP simulation package.[42,43] Strong interatomic distance potentials were applied to the B–B bonds, and bond-bending potentials were applied to the B–B–B angles within the octahedra. No other potentials were applied to the network, meaning that the octahedra can twist about the connecting B–B bonds with no energy cost. The metal atoms were not included in the model.

For a given phonon wave vector $\mathbf{k}$ and label i, we form the comparison of the phonon eigenvector $\mathbf{e}_i(\mathbf{k})$ from the full lattice dynamics calculation with the eigenvectors $\mathbf{e}'_j(\mathbf{k})$ for the flexibility model through the vector product relationship defined by Rimmer and Dove:[36]

$$m_i(\mathbf{k}) = \Omega^2 \sum_j \frac{\left|\mathbf{e}_i(\mathbf{k}) \cdot \mathbf{e}'_j(\mathbf{k})\right|}{\Omega^2 + \omega'^2_j(\mathbf{k})} \quad (2)$$

where $\omega'_j(\mathbf{k})$ is the (angular) frequency of the j-th mode in the model calculation, the sum is over all modes in the model calculation, and Ω is an arbitrary value designed simply to prevent divergence when $\omega'_j(\mathbf{k}) \simeq 0$, but because we needed to include forces for the motion of the metal atom the RUMs will

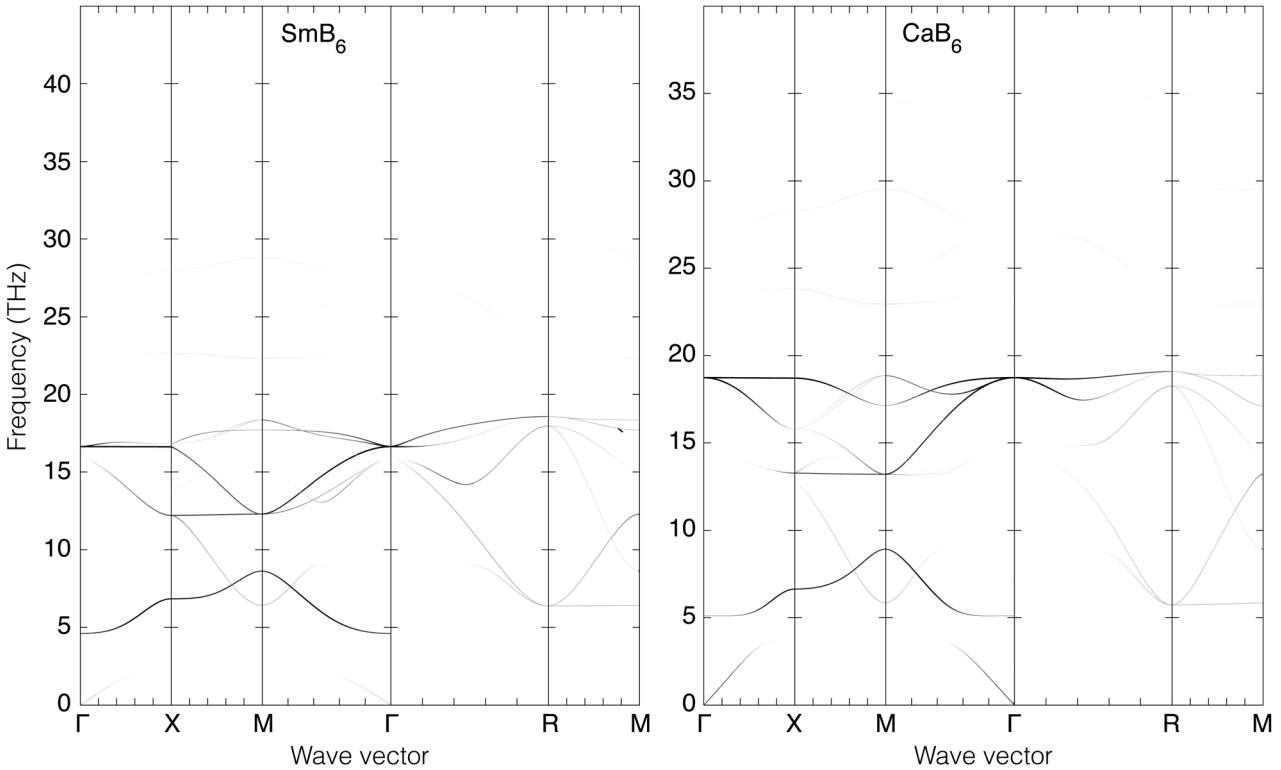

Fig. 5 Calculated phonon dispersion curves of SmB_6 (left) and CaB_6 (right) coloured between white and black to indicate the degree to which the mode eigenvectors can be described as a combination of the RUMs identified in a simple flexibility model, where black indicates close alignment of the phonon eigenvectors with the RUMs. The wave vector labels have conventional meaning: Γ represents the wave vector (0, 0, 0), X represents $(\frac{1}{2}, 0, 0)$, M represents $(\frac{1}{2}, \frac{1}{2}, 0)$ and R represents $(\frac{1}{2}, \frac{1}{2}, \frac{1}{2})$.

not quite have zero frequency so it was necessary that the value of Ω is significantly larger than the RUM frequencies. From the orthonormality of the phonon eigenvectors we have $m_i(\mathbf{k}) \leq 1$ for all modes. The case $m_i(\mathbf{k}) \sim 1$ corresponds to the case where there is a close matching of the eigenvector of the phonon in the full calculation to that of a RUM in the model calculation; in this case one of the products of the eigenvectors is close to a value of 1 and the frequency $\omega_j'(\mathbf{k}) \simeq 0$.

The results of the flexibility for SmB_6 and CaB_6 are shown in Fig. 5, where we plot the dispersion curves of Fig. 4 and shade the curves towards black where there is a perfect match between the phonon and RUM eigenvectors – where, in eqn (2), $m_i(\mathbf{k}) = 1$ – and white where there is no match ($m_i(\mathbf{k}) = 0$).

What we have previously noted is that when the phonon modes that are nominally RUMs are of low frequency, and separated from other modes, we see a clear RUM character.[18] However, when they are of higher frequency, or when there are other low-energy modes, the RUM eigenvectors can mix with those of other phonons. This has been discussed previously,[19] and is seen in the case of $Zn(CN)_2$ where the RUM eigenvectors are spread over a few modes with frequencies around that of the nominally-RUM phonon,[3] and in ZrW_2O_8 where there is a surface of RUMs in reciprocal space and such a broad distribution of phonon frequencies that the RUM is simply not visible at all.[8]

In Fig. 5 we see that the RUMs are identified with phonons of relatively high frequency, as in $Zn(CN)_2$.[3] In the latter case, this arises from the resistance of the chemical bonds against flexing of the linear Zn–C–N–Zn connection. This is in contrast to the analogous material $Si(NCN)_2$, which we have recently studied using an approach similar to the one here.[41] In that case, the Si–N–C linkage is much more flexible, and the RUMs are well separated from the frequencies of all other phonons and are clearly identified as such.

The high frequencies of the RUMs identified in Fig. 5 – see also the discussion of mode eigenvectors for phonons at zero wave vector in Section 3, where we identified the T_{1g} phonon as having RUM character – show that the torstional flexing of the B_6–B_6 linkage is of high energy, and thus the picture of freely-jointed B_6 octahedra is not represented in the phonon spectrum. This is unlike the case of the cubic perovskites, where there is clear evidence from calculated[44] and measured[45] phonon dispersion curves of a high degree of flexibility of the linked octahedra. In the case of perovskite the RUMs have wave vectors only along the line M–R in reciprocal space,[17] that is, for wave vectors between $(0, \frac{1}{2}, \frac{1}{2})$ and $(\frac{1}{2}, \frac{1}{2}, \frac{1}{2})$, and evidence from inelastic neutron scattering data and calculations show a low frequency along this branch. It is clear in the case of the metal hexaborides, Fig. 4 and 5, that the corresponding line in the dispersion curves does not show low frequencies.

We conclude from this analysis that in fact the network of connected B_6 octahedra does not have the flexibility seen in more traditional RUM systems such as cubic perovskites[17] and

phases of silica or silicates.[18] In fact this might have been anticipated from the data shown in Table 1 and Fig. 3. Incorporation of the larger cations causes the B_6 octahedra and their connecting B–B bonds to become strained, and hence the whole network will become more taut and less flexible.

5 Thermodynamic properties from vibrational spectra

The phonon densities of states of SmB_6 and CaB_6 are shown in Fig. 6a and b respectively, and corresponding data for SrB_6 and BaB_6 are given in the ESI.† The phonon densities of states show the gaps at frequencies of around 20 THz and just above 30 THz as seen in the phonon dispersion curves, Fig. 4. The same gaps are seen in SrB_6 and BaB_6.

Of relevance for the thermal expansion are the mode Grüneisen parameters γ_i as defined earlier in Section 2.3. We have computed these for a random set of wave vectors, and we plot a histogram of the distribution of values of γ as spread across the range of phonon frequencies. Fig. 6c and d show these distributions for SmB_6 and CaB_6 respectively, and corresponding data for SrB_6 and BaB_6 given in the ESI.† It is clear that there are phonons in SmB_6 and CaB_6 that have negative values of γ_i, but there are many more that have positive values, particularly at low frequency. However, in SrB_6 and BaB_6 there are many fewer phonons with negative values of γ.

Fig. 7 shows the distribution of significant values of γ across the dispersion curves of SmB_6 and CaB_6 shown in Fig. 4; corresponding diagrams for SrB_6 and BaB_6 are again given in the ESI.†

The overall Grüneisen parameters, $\bar{\gamma}$, of SmB_6, CaB_6, SrB_6 and BaB_6, as calculated from eqn (1), are shown as functions of temperature in Fig. 8. Not surprisingly, in the light of the data shown in Fig. 6, and of the corresponding data shown in the ESI,† even at low temperature the overall Grüneisen parameters

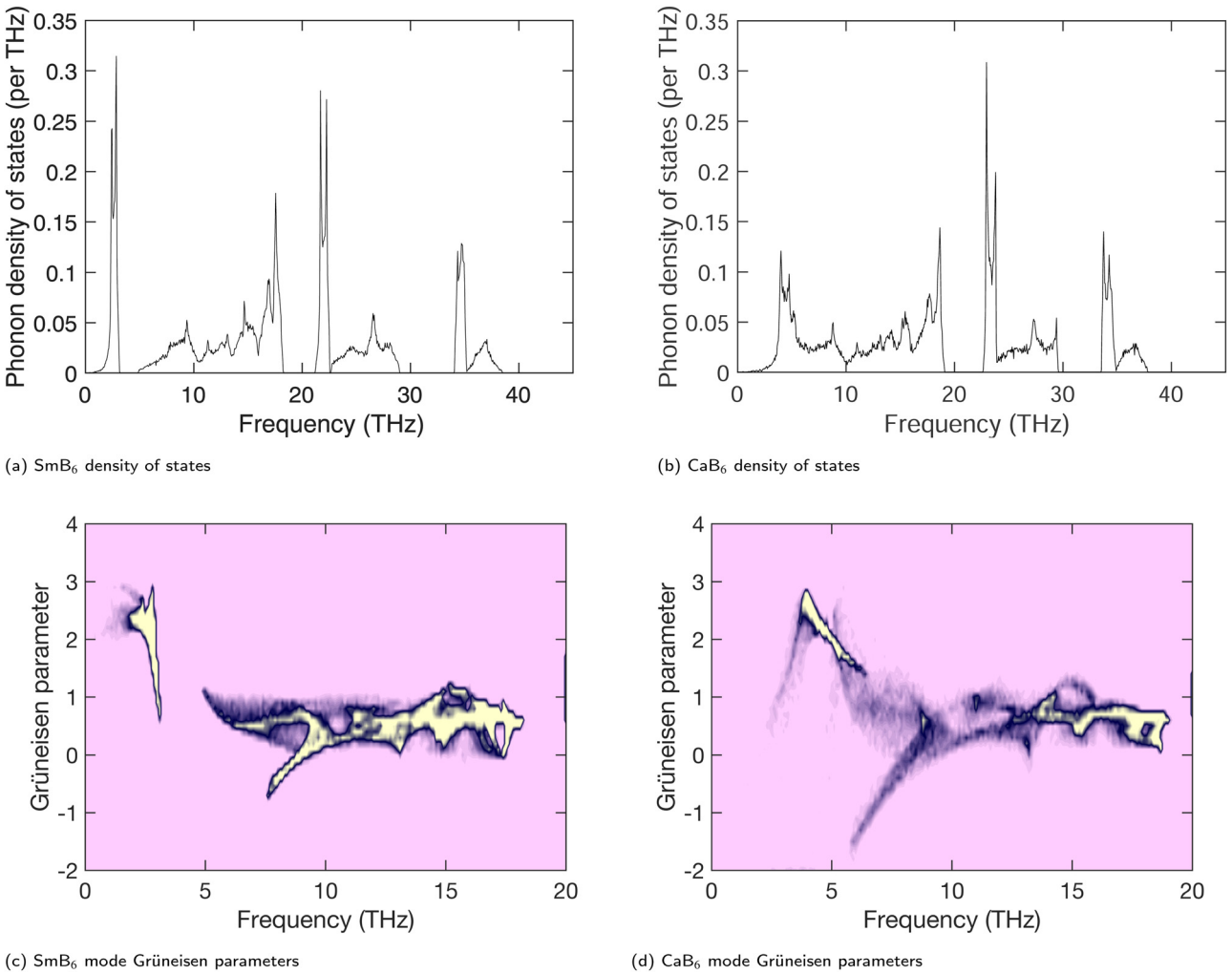

(a) SmB_6 density of states

(b) CaB_6 density of states

(c) SmB_6 mode Grüneisen parameters

(d) CaB_6 mode Grüneisen parameters

Fig. 6 Calculation of phonon densities of states for SmB_6 (a) and CaB_6 (b), and distribution of values of mode Grüeisen parameters across the range of frequencies for SmB_6 (c) and CaB_6 (d). In the latter two, pink represents a zero of phonon modes with a particular pair of values of frequency and Grüeisen parameters, yellow corresponds to the maximum in the distribution function, and the colour scheme passes from pink to yellow through dark blue. In order to highlight the existence of the distribution function for which there are fewer modes we saturate the scale of the histogram.

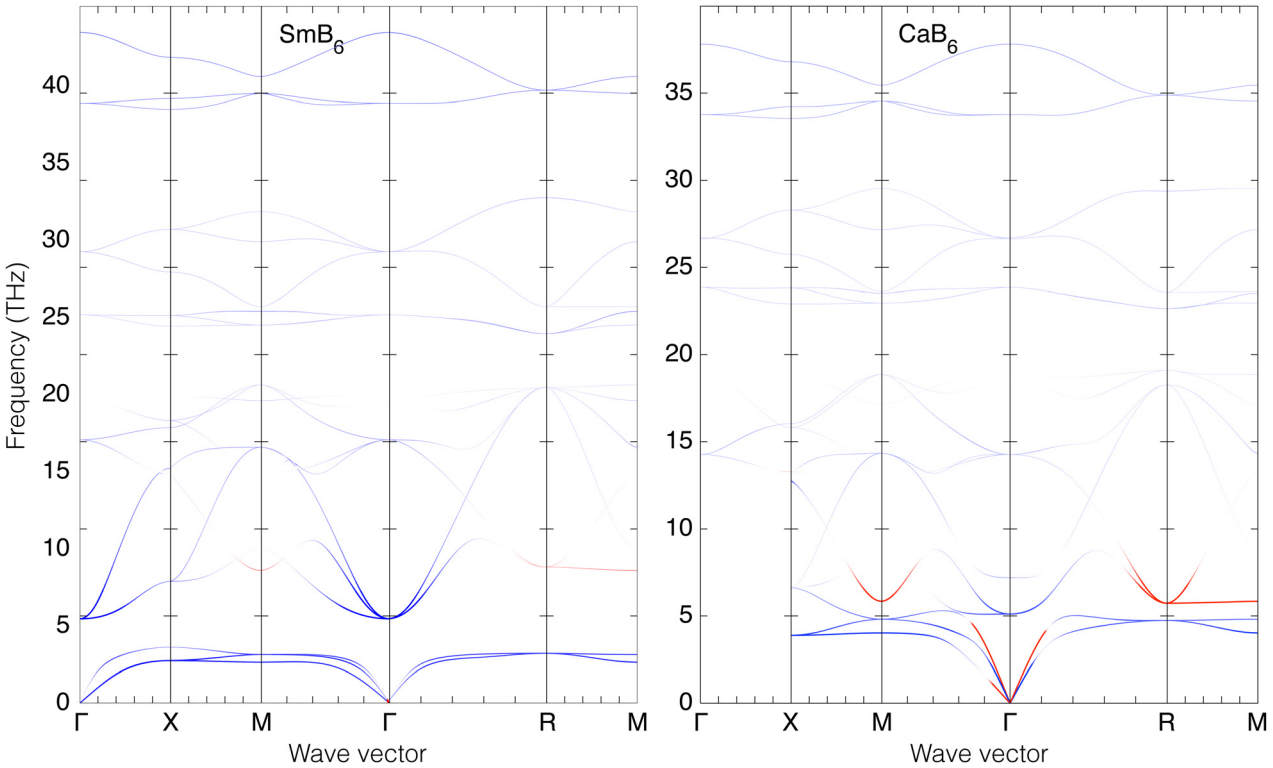

Fig. 7 Calculated phonon dispersion curves of SmB_6 (left) and CaB_6 (right) coloured between red and blue to indicate the values of the mode Grüneisen parameters γ_i, where the strongest red indicates values of $\gamma_i < -1$ and the strongest blue indicates values of $\gamma_i > +3$. The wave vector labels have conventional meaning: Γ represents the wave vector (0, 0, 0), X represents $(\frac{1}{2}, 0, 0)$, M represents $(\frac{1}{2}, \frac{1}{2}, 0)$ and R represents $(\frac{1}{2}, \frac{1}{2}, \frac{1}{2})$.

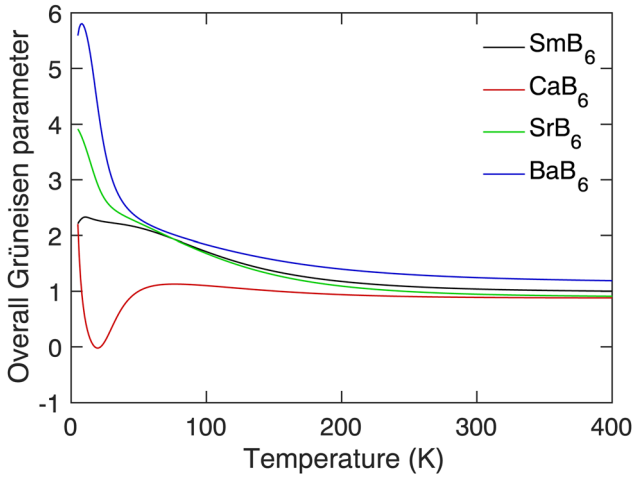

Fig. 8 Calculation of the temperature-dependence of the overall Grüneisen parameters of SmB_6, CaB_6, SrB_6 and BaB_6.

are dominated by the distribution of positive-valued mode Grüneisen parameters at low frequencies.

What we see is that in SrB_6 and BaB_6 there is not the slightest hint of a negative thermal expansion. On the other hand, CaB_6 does show negative thermal expansion for a small range of temperatures at low temperature as indicated by a negative value of $\bar{\gamma}$. The interesting case for us is SmB_6, which we have to conclude does not show negative thermal expansion as arising from the phonons. The accuracy of our calculated phonons is attested by the good agreement with the inelastic neutron scattering data shown in Fig. 4, and so we can conclude that the negative thermal expansion shown by the data in Fig. 2 must have a different origin that of the normal phonon mechanism.[8]

The values of the coefficients of volume thermal expansion for the four hexaborides, calculated as described in Section 2.3, are shown in Fig. 9. The data, of course, follow the trend seen in

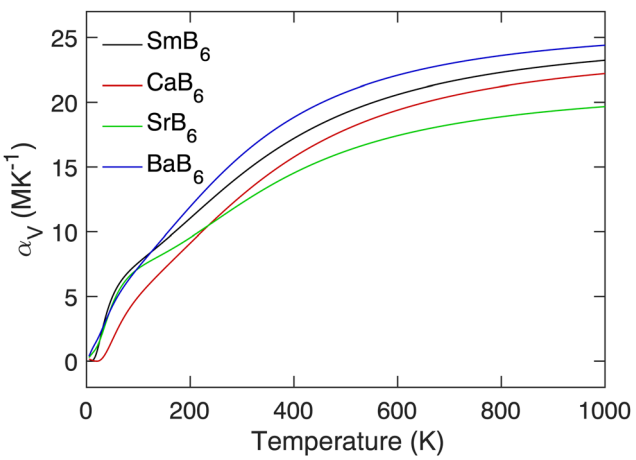

Fig. 9 Calculation of the temperature-dependence of the volume thermal expansion of SmB_6, CaB_6, SrB_6 and BaB_6.

the overall Grüneisen parameters (Fig. 8), with a small range of NTE seen in CaB_6 only.

6 Discussion

The work of this paper has been concerned with analysing the flexibility of the network of connected B_6 octahedra in simple cubic metal hexaborides. The key finding from the DFT phonon calculations presented here is that in each case the network is not particularly flexible, with an energy cost to flex the orientation of one B_6 octahedron about the linkage B–B bond connecting two tetrahedra. This was seen in the calculation of RUMs, where their frequencies are far from being low. As a result, we concluded that the NTE observed in SmB_6 (Fig. 2) does not have its origin in the tension effect and phonons. On the other hand, there is a weak effect in CaB_6 which would be interesting to investigate using low-temperature diffraction methods.

The methods employed in this study are based on the quasi-harmonic model of Grüneisen in which the important anharmonic effects are coupling of interatomic force constants with volume. It might be asked whether NTE could arise if account were taken of direct phonon–phonon anharmonic interactions as accounted for, for example, in renormalised phonon theory. Most evidence, and in this we include our own theoretical study that addresses this point exactly,[46] is that anharmonic effects will lower the magnitude of the mode Grüneisen parameters of the renormalised phonons because their frequency will increase, and cannot change the sign of mode Grüneisen parameters from positive to negative. We do not believe that there is evidence to suggest that the current state of anharmonic phonon theory will indicate that there is a possibility to find NTE when Grüneisen theory doesn't show NTE.

It is known that there are electronic mechanisms for NTE,[47] whether directly so or *via* magnetic interactions. In this regard, we note that although the samarium atom is magnetic, magnetic ordering in SmB_6 has been shown to be absent down to a temperature of 19 mK.[21] Thus in our calculations we did not include magnetic interactions, and the good agreement of our calculated phonon dispersion curves with experimental data shows that this was reasonable. It is also observed that samples of the alkali-earth hexaborides can show magnetism, but this is believed to have its origin in a mechanism that is not directly a bulk property, such as broken B–B bonds at surfaces and interfaces, and magnetism of B_6 octahedra without saturated connectivity.[48]

In our calculations on SmB_6 we attempted to investigate effects of electron entropy through calculation of changes of electron entropy with volume. However, in our calculations on SmB_6 we observed that electron entropy consistently increases with volume across a range of Fermi-Dirac smearing temperatures from 100–1000 K, which means the electron entropy favours positive thermal expansion just as the phonon entropy does. Recently one of us (LL) had calculated the band structure for a range of volumes,[49] showing that over a contraction of several percent there is no clear change in the electronic density of states.

At this point we are forced to conclude that the NTE in SmB_6 remains of unknown origin.

Author contributions

Li Li: investigation, formal analysis, validation, writing (review & editing), visualisation. Keith Refson: software, writing (review & editing). Martin T Dove: conceptualisation, methodology, software, validation, formal analysis, resources, writing (original draft), visualisation, supervision, funding acquisition.

Conflicts of interest

There are no conflicts to declare.

Acknowledgements

We acknowledge financial support from National Natural Science Foundation of China, grant number 12174274 (MTD). This research made use of the Apocrita HPC facility of Queen Mary University of London, supported by QMUL Research-IT and initially funded by EPSRC grants EP/K000128/1 and EP/K000233/1 (MTD), and the EPSRC-funded HPC Midlands Plus (EP/P020232/1) Tier-2 system, which we accessed as members of the project consortium (MTD).

References

1 V. A. Trounov, A. L. Malyshev, D. Y. Chernyshov, M. M. Korsukova, V. N. Gurin, L. A. Aslanov and V. V. Chernyshev, *J. Phys.: Condens. Matter*, 1999, **5**, 2479–2488.
2 C.-H. Chen, T. Aizawa, N. Iyi, A. Sato and S. Otani, *J. Alloys Compd.*, 2004, **366**, L6–L8.
3 H. Fang, M. T. Dove, L. H. N. Rimmer and A. J. Misquitta, *Phys. Rev. B*, 2013, **88**, 104306.
4 T. Matsuda, J. E. Kim, K. Ohoyama and Y. Moritomo, *Phys. Rev. B*, 2009, **79**, 172302–172304.
5 S. Adak, L. L. Daemen, M. Hartl, D. Williams, J. Summerhill and H. Nakotte, *J. Solid State Chem.*, 2011, **184**, 2854–2861.
6 C. Lind, *Materials*, 2012, **5**, 1125–1154.
7 J. Chen, L. Hu, J. Deng and X. Xing, *Chem. Soc. Rev.*, 2015, **44**, 3522–3567.
8 M. T. Dove and H. Fang, *Rep. Prog. Phys.*, 2016, **79**, 066503.
9 R. Mittal, M. K. Gupta and S. L. Chaplot, *Prog. Mater. Sci.*, 2018, **92**, 360–445.
10 N. Shi, Y. Song, X. Xing and J. Chen, *Coord. Chem. Rev.*, 2021, **449**, 214204.
11 T. Chatterji, P. Henry, R. Mittal and S. Chaplot, *Phys. Rev. B*, 2008, **78**, 134105.
12 M. Dapiaggi and A. N. Fitch, *J. Appl. Crystallogr.*, 2009, **42**, 253–258.

13 B. K. Greve, K. L. Martin, P. L. Lee, P. J. Chupas, K. W. Chapman and A. P. Wilkinson, *J. Am. Chem. Soc.*, 2010, **132**, 15496–15498.
14 L. Hu, J. Chen, A. Sanson, H. Wu, C. Guglieri Rodriguez, L. Olivi, Y. Ren, L. Fan, J. Deng and X. Xing, *J. Am. Chem. Soc.*, 2016, **138**, 8320–8323.
15 T. A. Mary, J. S. O. Evans, T. Vogt and A. W. Sleight, *Science*, 1996, **272**, 90–92.
16 M. T. Dove, J. Du, Z. Wei, D. A. Keen, M. G. Tucker and A. E. Phillips, *Phys. Rev. B*, 2020, **102**, 094105.
17 A. P. Giddy, M. T. Dove, G. S. Pawley and V. Heine, *Acta Crystallogr., Sect. A: Found. Crystallogr.*, 1993, **49**, 697–703.
18 K. D. Hammonds, M. T. Dove, A. P. Giddy, V. Heine and B. Winkler, *Am. Mineral.*, 1996, **81**, 1057–1079.
19 M. T. Dove, *Philos. Trans. R. Soc., A*, 2019, **377**, 20180222.
20 I. Batko and M. Batkova, *Solid State Commun.*, 2014, **196**, 18–23.
21 P. K. Biswas, Z. Salman, T. Neupert, E. Morenzoni, E. Pomjakushina, F. von Rohr, K. Conder, G. Balakrishnan, M. C. Hatnean, M. R. Lees, D. M. Paul, A. Schilling, C. Baines, H. Luetkens, R. Khasanov and A. Amato, *Phys. Rev. B*, 2014, **89**, 155.
22 J. C. Cooley, M. C. Aronson, A. Lacerda, P. C. Canfield, Z. Fisk and R. P. Guertin, *Phys. B*, 1995, **206–207**, 377–379.
23 S. Gabáni, E. Bauer, M. Della Mea, K. Flachbart, Y. Paderno, V. Pavlík and N. Shitsevalova, *J. Magn. Magn. Mater.*, 2004, **272–276**, 397–399.
24 F. Lu, J. Zhao, H. Weng, Z. Fang and X. Dai, *Phys. Rev. Lett.*, 2013, **110**, 096401.
25 P. Nyhus, S. L. Cooper, Z. Fisk and J. Sarrao, *Phys. Rev. B*, 1997, **55**, 12488–12496.
26 P. S. Riseborough, *Adv. Phys.*, 2000, **49**, 257–320.
27 P. Syers, D. Kim, M. S. Fuhrer and J. Paglione, *Phys. Rev. Lett.*, 2015, **114**, 096601.
28 B. S. Tan, Y. T. Hsu, B. Zeng, M. C. Hatnean, N. Harrison, Z. Zhu, M. Hartstein, M. Kiourlappou, A. Srivastava, M. D. Johannes, T. P. Murphy, J. H. Park, L. Balicas, G. G. Lonzarich, G. Balakrishnan and S. E. Sebastian, *Science*, 2015, **349**, 287–290.
29 S. J. Clark, M. D. Segall, C. J. Pickard, P. J. Hasnip, M. I. J. Probert, K. Refson and M. C. Payne, *Z. Kristallogr. - Cryst. Mater.*, 2005, **220**, 191–194.
30 J. P. Perdew, K. Burke and M. Ernzerhof, *Phys. Rev. Lett.*, 1996, **77**, 3865–3868.
31 J. P. Perdew, K. Burke, M. Ernzerhof and R. Ernstorfer, *Phys. Rev. Lett.*, 1997, **78**, 1396.
32 H. J. Monkhorst and J. D. Pack, *Phys. Rev. B*, 1976, **13**, 5188–5192.
33 K. Schmitt, C. Stückl, H. Ripplinger and B. Albert, *Solid State Sci.*, 2001, **3**, 321–327.
34 S. Baroni, S. de Gironcoli and A. D. Corso, *Rev. Mod. Phys.*, 2001, **73**, 515–562.
35 K. Refson, P. R. Tulip and S. J. Clark, *Phys. Rev. B*, 2006, **73**, 155114.
36 L. H. N. Rimmer and M. T. Dove, *J. Phys.: Condens. Matter*, 2015, **27**, 185401.
37 P. A. Alekseev, A. S. Ivanov, B. Dorner, H. Schober, K. A. Kikoin, A. S. Mishchenko, V. N. Lazukov, E. S. Konovalova, Y. B. Paderno, A. Y. Rumyantsev and I. P. Sadikov, *Europhys. Lett.*, 2007, **10**, 457–463.
38 N. Ogita, S. Nagai, N. Okamoto, F. Iga, S. Kunii, T. Akamtsu, J. Akimitsu and M. Udagawa, *J. Solid State Chem.*, 2004, **177**, 461–465.
39 I. Mörke, V. Dvorák and P. Wachter, *Solid State Commun.*, 1981, **40**, 331–334.
40 A. L. Goodwin, *Phys. Rev. B*, 2006, **74**, 134302.
41 L. Li, K. Refson and M. T. Dove, *J. Phys.: Condens. Matter*, 2020, **32**, 465402.
42 J. D. Gale, *J. Chem. Soc., Faraday Trans.*, 1997, **93**, 629–637.
43 J. D. Gale and A. L. Rohl, *Mol. Simul.*, 2003, **29**, 291–341.
44 C. W. Li, X. Tang, J. A. Muñoz, J. B. Keith, S. J. Tracy, D. L. Abernathy and B. Fultz, *Phys. Rev. Lett.*, 2011, **107**, 195504.
45 W. G. Stirling, *J. Phys. C: Solid State Phys.*, 1972, **5**, 2711–2730.
46 H. Fang and M. T. Dove, *Phys. Rev. B*, 2013, **87**, 214109.
47 J. P. Attfield, *Front. Chem.*, 2018, **6**, 14441–14446.
48 R. Monnier and B. Delley, *Phys. Rev. Lett.*, 2001, **87**, 157204.
49 L. Li, C.-E. Hu, M. Tang, Y. Cheng and G.-F. Ji, *Philos. Mag.*, 2017, **97**, 1144–1156.

